

# Rydberg atom arrays as quantum simulators for molecular dynamics

Simon Euchner<sup>1</sup> and Igor Lesanovsky<sup>1, 2</sup>

<sup>1</sup>*Institut für Theoretische Physik and Center for Integrated Quantum Science and Technology, Universität Tübingen, Auf der Morgenstelle 14, 72076 Tübingen, Germany*

<sup>2</sup>*School of Physics and Astronomy and Centre for the Mathematics and Theoretical Physics of Quantum Non-Equilibrium Systems, The University of Nottingham, Nottingham, NG7 2RD, United Kingdom*

Rydberg atoms held in optical tweezer arrays combine vibrational and electronic degrees of freedom which can be coupled and manipulated at a microscopic level. This opens opportunities for the quantum simulation of artificial molecular systems and offers in particular a platform for probing complex vibronic dynamics in controlled settings with increasing complexity. Tailored interatomic interactions and electron-phonon couplings yield handles for designing electronic state manifolds, for studying structural transitions, and for exploring non-classical vibrational states near molecular instabilities. Furthermore, this quantum simulator opens opportunities for testing and quantifying the validity of fundamental concepts, such as the Born-Oppenheimer approximation and quantum corrections to it.

*Introduction.*—Shedding light on dynamical processes within molecules is essential for many problems in physics, chemistry, and biology [1–4]. However, their coupled electronic and motional degrees of freedoms typically result in a high-dimensional state space that makes *ab initio* calculations forbiddingly complex [5]. This is particularly the case when common simplifications, such as the adiabatic approximation [6], for computing electronic potential surfaces are not applicable. An important example in this regard is the process of human vision which relies on a conformational change of molecular structure near crossing potential surfaces [7, 8]. This and other related processes take place usually on an Angstrom length scale and on a femtosecond time scale. One approach to study them at directly observable length and drastically prolonged time scales — and thereby to shed light on their physics — is to use quantum simulators [9, 10]. Initial steps into this direction have already been undertaken: trapped ion setups have been used to mimic molecular dynamics near so-called conical intersections [11–13]. Rydberg atoms have been employed to create macroscopically large Rydberg molecules [14–20] as well as aggregates and clusters [21, 22]. The latter were probed using the van der Waals explosion [23], in analogy to the Coulomb explosion [24], which is a means to infer molecular structure.

In this paper, we showcase the potential of neutral atom arrays in optical tweezers [25–29] to serve as a quantum simulation platform for the study of molecular processes. To illustrate the capabilities of the simulator we focus on three elementary molecular shapes of increasing complexity — a dumbbell, a triangle, and a tetrahedron. Already these simple examples reveal a range of intriguing properties, such as the emergence of motional instabilities and non-classical, i.e., squeezed, vibrational ground states. The platform furthermore offers the capability of designing the structure of the electronic state space. More broadly, it allows to system-

atically investigate the impact of quantum effects, which become particularly important in regimes where the commonly used Born-Oppenheimer approximation (BOA) [6] breaks down. Rydberg tweezer arrays allow to quantitatively test the applicability of such approximations and to perform fully quantum mechanical investigations of molecular processes in system sizes that are intractable by exact numerical methods.

*Molecular quantum simulator.*—We consider  $N$  optical tweezers, each confining a single atom [see examples in Fig. 1(a-c)]. The dynamics of a single atom trapped in the  $k$ -th tweezer is described by the single atom Hamiltonian ( $\hbar \equiv 1$ )

$$H^{(k)} = \Omega \sigma_x^{(k)} + \Delta n^{(k)} + \omega \sum_{j=x,y,z} (a_j^{(k)})^\dagger a_j^{(k)}. \quad (1)$$

The first two terms, with  $\sigma_x = |\downarrow\rangle\langle\uparrow| + |\uparrow\rangle\langle\downarrow|$  and  $n = |\uparrow\rangle\langle\uparrow|$ , model a laser which drives transitions between the ground ( $|\downarrow\rangle$ ) and Rydberg ( $|\uparrow\rangle$ ) state with Rabi frequency  $\Omega$  and detuning  $\Delta$  [cf. Fig. 1(a)]. The second term describes the vibrations of the atom in the tweezer relative to its equilibrium position. Here, the phonon annihilation operators,  $a_j^{(k)}$ , represent the corresponding displacements  $\delta r_j^{(k)} = x_0 (a_j^{(k)} + (a_j^{(k)})^\dagger) / \sqrt{2}$  in direction  $j = x, y, z$  [see Fig. 1(c)], and  $x_0 = 1/\sqrt{m\omega}$  is the harmonic oscillator length. For simplicity, we assume the tweezer potentials to be isotropic and electronic state-independent [30, 31]. The full many-body Hamiltonian of the tweezer array is

$$H = \sum_{k=1}^N H^{(k)} + \sum_{k=1}^N \sum_{l=1}^{k-1} V(r^{(k,l)}) n^{(k)} n^{(l)}, \quad (2)$$

where  $V(r^{(k,l)})$  describes interactions between Rydberg atoms as a function of the distance  $r^{(k,l)}$  between the  $k$ -th and  $l$ -th atom. Typically, the interaction potential follows a power-law [32–34]. However, using Förster resonances and microwave dressing allows one to create a

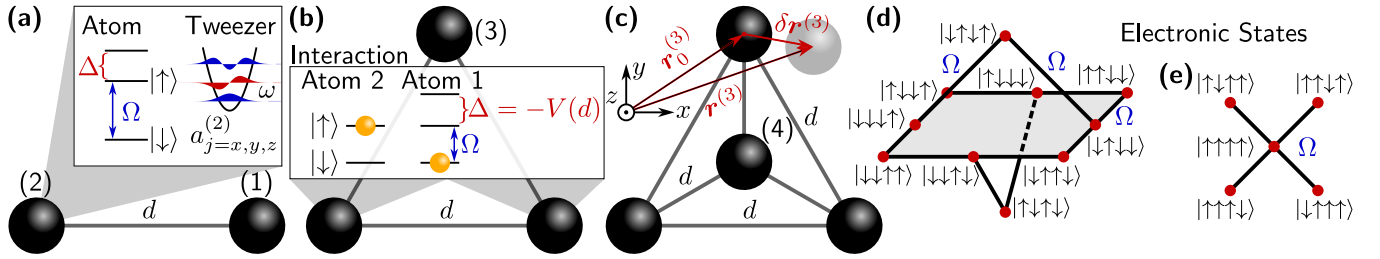


Figure 1. *Atom tweezer arrays and electronic state space.* (a) Dumbbell-shaped atom array. Atoms are modeled by a two-level system with states  $|\downarrow\rangle$  (ground state) and  $|\uparrow\rangle$  (Rydberg state). Transitions are driven by a laser with detuning  $\Delta$  and Rabi frequency  $\Omega$ . The tweezer confinement is modelled by a harmonic oscillator with trapping frequency  $\omega$  and phonon annihilation operators  $a_j^{(k)}$  for the directions  $j = x, y, z$ . The superscript  $k$  labels the atom in the array. The atomic equilibrium positions of the dumbbell are  $\mathbf{r}_0^{(1)} = d(1, 0, 0)^T$  and  $\mathbf{r}_0^{(2)} = d(0, 0, 0)^T$ . (b) Triangular atom array, obtained by extending the dumbbell with a third atom at position  $\mathbf{r}_0^{(3)} = d(1/2, \sqrt{3}/2, 0)^T$ . If atom 2 is in its Rydberg state, the Rydberg state of atom 1 experiences the interaction energy shift  $V(d)$ . When the laser detuning cancels this interaction shift,  $\Delta = -V(d)$ , atom 1 undergoes a facilitated excitation. (c) Tetrahedral atom array, obtained from the triangle [see (b)] by adding an atom at position  $\mathbf{r}_0^{(4)} = d(1/2, 1/(2\sqrt{3}), \sqrt{2}/3)^T$ . The position  $\mathbf{r}^{(k)} = \mathbf{r}_0^{(k)} + \delta\mathbf{r}^{(k)}$  of the  $k$ -th atom in the array is the sum of the equilibrium position  $\mathbf{r}_0^{(k)}$  and the displacement vector  $\delta\mathbf{r}^{(k)}$ , with components  $\delta\mathbf{r}_j^{(k)} = x_0(a_j^{(k)} + (a_j^{(k)})^\dagger)/\sqrt{2}$ . (d,e) Visualization of coupled (at rate  $\Omega$ ) resonant electronic states of the tetrahedron. The graph in (d) emerges when choosing the facilitation condition  $\Delta = -V(d)$ , and (e) is obtained when setting  $\Delta = -3V(d)$ .

variety of shapes [35–37], including Lennard-Jones type potentials with repulsive core and attractive long-range tail. Typical atom equilibrium distances in tweezer arrays are  $d \approx 3\text{--}6 \mu\text{m}$  [38–40] and trap frequencies can be on the order of  $\omega = 100 \text{ kHz} \approx 2\pi \cdot 16 \text{ kHz}$ . For  ${}^7\text{Li}$  atoms this yields a harmonic oscillator length of  $x_0 = 1/\sqrt{\omega m} \approx 300 \text{ nm}$  and hence a ratio between atomic displacement and interatomic separation of  $\nu = x_0/d \lesssim 0.1$ . Close to the vibrational ground state this justifies the following expansion of the interaction potential

$$V(r^{(k,l)}) \approx V(r_0^{(k,l)}) + \mathbf{G}^{(k,l)} \delta\mathbf{r}^{(k,l)} + \frac{1}{2} (\delta\mathbf{r}^{(k,l)})^T (H_a^{(k,l)} + H_b^{(k,l)}) \delta\mathbf{r}^{(k,l)}, \quad (3)$$

with  $\delta\mathbf{r}^{(k,l)} = \delta\mathbf{r}^{(k)} - \delta\mathbf{r}^{(l)}$ . Here the second and third term couple the electronic state-dependent interaction to the vibrations of the atoms inside the tweezer potential. The strength and nature of this vibronic coupling is quantified by the expansion coefficients

$$\mathbf{G}^{(k,l)} = V'(r_0^{(k,l)}) \frac{(\mathbf{r}_0^{(k,l)})^T}{r_0^{(k,l)}}, \quad (4)$$

$$H_a^{(k,l)} = V''(r_0^{(k,l)}) \frac{\mathbf{r}_0^{(k,l)}}{r_0^{(k,l)}} \otimes \frac{(\mathbf{r}_0^{(k,l)})^T}{r_0^{(k,l)}}, \quad (5)$$

$$H_b^{(k,l)} = \frac{V'(r_0^{(k,l)})}{r_0^{(k,l)}} \left[ \mathbf{1}_3 - \frac{\mathbf{r}_0^{(k,l)}}{r_0^{(k,l)}} \otimes \frac{(\mathbf{r}_0^{(k,l)})^T}{r_0^{(k,l)}} \right], \quad (6)$$

where  $\mathbf{r}_0^{(k,l)} = \mathbf{r}_0^{(k)} - \mathbf{r}_0^{(l)}$  denotes the distance vector between equilibrium positions and  $r_0^{(k,l)} = \|\mathbf{r}_0^{(k,l)}\|$ .

*Molecular Hamiltonians.*—To get a first impression of the capabilities of the simulator we first focus on the

dumbbell depicted in Fig. 1(a). In order to simplify the problem we employ the facilitation condition  $\Delta = -V(d)$  and  $|\Delta| \gg |\Omega|$  [41–46] [see Fig. 1(b)]. This splits the electronic Hilbert space into two approximately decoupled [47] manifolds of resonant states:  $\{|\downarrow\downarrow\rangle\}$  and  $\{|\downarrow\uparrow\rangle, |\uparrow\downarrow\rangle, |\uparrow\uparrow\rangle\}$ , with energy separation  $|\Delta|$ . Only the latter one features vibronic couplings. Here, the constrained [48–50] electronic dynamics can be represented by a tight-binding model on a graph, where  $\Omega$  is the coherent hopping rate between nodes:  $|\downarrow\uparrow\rangle \xleftrightarrow{\Omega} |\uparrow\uparrow\rangle \xleftrightarrow{\Omega} |\uparrow\downarrow\rangle$ . In fact a further simplification is achieved by introducing the state  $|\rangle = (|\downarrow\uparrow\rangle + |\uparrow\downarrow\rangle)/\sqrt{2}$ , which restricts the electronic dynamics to the space  $\{|\rangle, |\uparrow\uparrow\rangle\}$ . Furthermore, introducing the vibrational mode of the relative motion,  $b = (a^{(1)} - a^{(2)})/\sqrt{2}$ , yields the following compact matrix representation of the dumbbell Hamiltonian:

$$H_2 = \begin{bmatrix} \omega b^\dagger b & \sqrt{2}\Omega \\ \sqrt{2}\Omega & \omega b^\dagger b + \sqrt{2}\kappa(b + b^\dagger) + \xi(b + b^\dagger)^2 \end{bmatrix}. \quad (7)$$

Here, we defined the vibronic coupling constants  $\kappa = x_0 V'(d)/\sqrt{2}$  and  $\xi = x_0^2 V''(d)/2$  which depend on the interaction potential gradient and curvature at the interatomic equilibrium distance  $d$ . This Hamiltonian illustrates the general idea behind the quantum simulator of molecular phenomena: diagonal entries describe the motion of “nuclear” degrees of freedom in electronic potential energy surfaces, which are a combination of the tweezer trap and the state-dependent interaction potential. These surfaces are hybridized by the off-diagonal entries due to the laser coupling with Rabi frequency  $\Omega$ . In general, the shape of the Hamiltonian can thus be engineered by controlling the Rydberg interaction poten-

tial  $V$ , i.e., through  $\kappa$  and  $\xi$ , the structure of the electronic state space, and the geometric arrangement of the tweezers. To illustrate this further, we consider next the tetrahedron depicted in Fig. 1(c). More atoms yield a larger electronic Hilbert space and choosing the laser detuning  $\Delta$  allows to engineer different graphs of resonant electronic states: setting  $\Delta = -V(d)$  yields the multiple-connected graph in Fig. 1(d) and setting  $\Delta = -3V(d)$  leads to the star graph shown in Fig. 1(e). Generally, the emerging vibronic Hamiltonians take the form

$$H_{\text{mol}} = \Omega \sum_{ss'} A_{ss'} |s\rangle\langle s'| + \sum_s h_s |s\rangle\langle s|, \quad (8)$$

where the matrix  $A$  is the adjacency matrix of the graph representing the electronic states that are resonantly connected by the laser. Furthermore, the Hamiltonians  $h_s$  model the electronic state-dependent vibrational “nuclear” dynamics. For the particular case of the tetrahedron and the graph in Fig. 1(d)  $A$  is ten-dimensional and the indices  $s$  and  $s'$  run over all electronic states contained in the graph. In states containing one Rydberg excitation vibrations are solely governed by the tweezer confinement:  $h_s = \omega \mathbf{b}_s^\dagger \mathbf{b}_s$ , where we collected all modes in the vector  $\mathbf{b}_s$ . States containing two Rydberg atoms feature a significantly more complex vibrational dynamics, which is governed by

$$h_s = \omega \mathbf{b}_s^\dagger \mathbf{b}_s + \sqrt{2}\kappa(b_s^\parallel + (b_s^\parallel)^\dagger) + \xi(b_s^\parallel + (b_s^\parallel)^\dagger)^2 + \frac{\nu\kappa}{\sqrt{2}}(b_s^{\perp,1} + (b_s^{\perp,1})^\dagger)^2 + \frac{\nu\kappa}{\sqrt{2}}(b_s^{\perp,2} + (b_s^{\perp,2})^\dagger)^2. \quad (9)$$

The parallel modes describe displacements along the tetrahedron’s edges, analogously to  $b$  in Eq. (7). The perpendicular modes govern motion within the plane perpendicular to each edge. For details see the supplemental material [51].

*Molecular instabilities and ground state squeezing.*— Let us now discuss some phenomena which can be explored with the quantum simulator. To this end we return to the dumbbell in Eq. (7) and consider the limit  $\Omega \rightarrow 0$ . Here the Hamiltonian can be diagonalized by a state-dependent Bogoliubov transformation (BT). In the  $|+\rangle$ -state this is trivial, whereas in the  $|\uparrow\uparrow\rangle$ -state we have the transformed mode (see supplemental material [51])  $b_{\text{BT}} = (b + wb^\dagger)/\sqrt{1 - w^2}$ , where

$$w = 1 + \phi - \frac{\phi}{|\phi|} \sqrt{(1 + \phi)^2 - 1}, \quad \phi = \frac{\omega}{2\xi}. \quad (10)$$

Crucially,  $w$  exists only if  $\xi > \xi_c$ , where  $\xi_c = -\omega/4$  is the critical potential curvature. Outside this regime the electron-phonon coupling renders the system unstable. This becomes also apparent from the molecular ground state energy (MGSE), which for  $\Omega = 0$  reads  $E_{\text{GS},2} = \min\{\omega\varepsilon_2, 0\}$ , with

$$\varepsilon_2 = -\frac{2\kappa^2}{\omega^2} \frac{1}{1 - \bar{\xi}} + \frac{1}{2} \sqrt{1 - \bar{\xi}} - \frac{1}{2}, \quad \bar{\xi} = \frac{\xi}{\xi_c}. \quad (11)$$

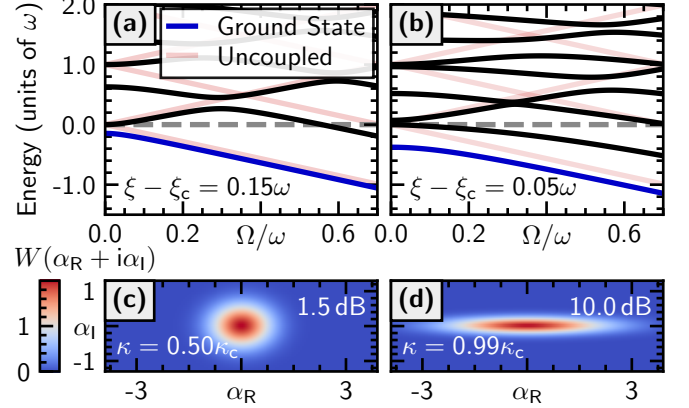


Figure 2. *Energy spectrum and Wigner distribution.* (a,b) Energy spectrum (black) of the dumbbell [Fig. 1(a)] as a function of the Rabi frequency  $\Omega$ . The spectrum is computed by exact diagonalization of Eq. (7) with  $\kappa = 0.1\omega$  and truncating at 100 phonons. In blue, we highlight the ground state. As a reference we show the uncoupled ( $\kappa = \xi = 0$ ) spectrum (red). (c,d) Wigner quasiprobability distribution of the ground state of the tetrahedron [Fig. 1(c)], Eq. (13), for different values of  $\kappa$ . We choose  $\xi = 2\omega$  and  $\nu = 0.1$ . In the top right the squeezing strengths (variance of the position quadrature associated to the mode with annihilation operator  $b_{|\uparrow\uparrow\downarrow\downarrow\rangle}^{\perp,1}$  normalized to the variance for  $\kappa = \xi = 0$ ) are shown.

At  $\xi = \xi_c$  the denominator of the first term vanishes and the energy diverges. For finite  $\Omega$ , we computed the MGSE numerically, which is shown as the blue curve in Fig. 2(a,b). Clearly, the ground state energy is lowered as  $|\xi - \xi_c|$  decreases and achieving numerical convergence becomes increasingly difficult as the instability is approached. In fact, the instability at  $\xi_c$  is expected to occur for arbitrary Rabi frequencies  $\Omega$  because Eq. (10) does not depend on  $\Omega$ . Physically, we understand the instability at  $\xi_c$  as the consequence of the trapping potential being canceled by the quadratic perturbations of the harmonic oscillator in Eq. (7). This is a somewhat trivial effect. The tetrahedron on the other hand features a second, in fact more interesting, instability which we find upon inspection of its ground state energy (at  $\Omega = 0$ ). It is given by  $E_{\text{GS},4} = \min\{\omega\varepsilon_4, 0\}$ , with

$$\varepsilon_4 = -\frac{2\kappa^2}{\omega^2} \frac{1}{1 - \bar{\xi}} + \frac{1}{2} \sqrt{1 - \bar{\xi}} + \sqrt{1 - \bar{\kappa}} - \frac{3}{2}, \quad \bar{\kappa} = \frac{\kappa}{\kappa_c}. \quad (12)$$

This expression is obtained by employing the BT defined by Eq. (10) to the Hamiltonians  $h_s$  in the state space contained in the graph of Fig. 1(d). A direct inspection shows that, in addition to the instability at  $\xi_c$ , we obtain a second one at  $\kappa_c = -\omega/(2\sqrt{2}\nu)$ , manifesting in an imaginary square root when  $\kappa < \kappa_c$ . This second instability can be characterized through the squeezing of the ground state wave function: for  $\Omega = 0$  a ground state of Eq. (8) is the product  $|\uparrow\uparrow\downarrow\downarrow\rangle \otimes |\text{GS}\rangle$ , where  $|\text{GS}\rangle$  is the ground state of  $h_{|\uparrow\uparrow\downarrow\downarrow\rangle}$  defined in Eq. (9). Its Wigner

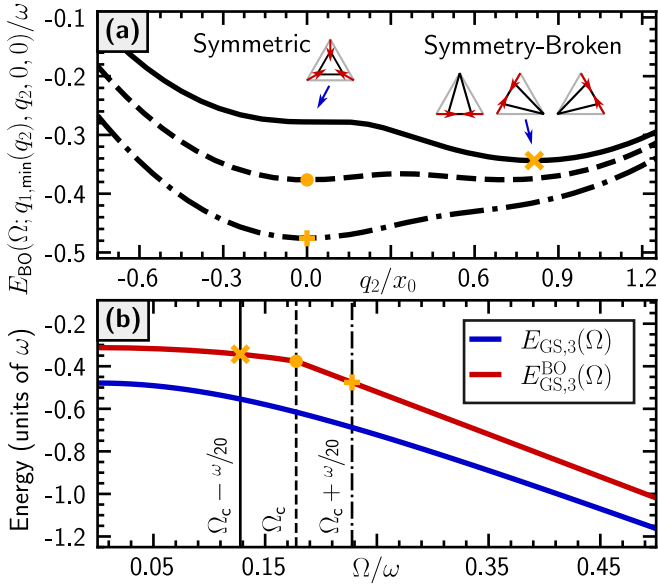


Figure 3. *Potential energy surfaces and ground state energy.* (a) Ground state potential energy surface for the triangle shown in Fig. 1(b). We plot the surface in the vicinity of one of the three-fold degenerate minima; the one that is associated with configurations in the vicinity of the leftmost of the three deformed triangular shapes. For  $\Omega = 0$  this surface is given by Eq. (14). The curves shown here are  $E_{\text{BO}}(\Omega; q_1, \min(q_2), q_2, q_3 = 0, q_4 = 0)$ , and the minimum of each curve (see yellow markers) corresponds to the ground state within the BOA for a given  $\Omega$ . At  $\Omega = \Omega_c$  a structural transition between a symmetric and a symmetry-broken triangle takes place (dashed line). For details see the supplemental material [51]. For the electron-phonon coupling parameters we chose  $\xi = -0.15\omega$ ,  $\kappa = 0.25\omega$ , and  $\nu = 0.1$ . (b) Ground state energy of the triangle as a function of the Rabi frequency  $\Omega$ . The curve  $E_{\text{GS},3}$  (blue) is obtained by exact diagonalization (truncated at 20 phonons per mode). The red curve shows the ground state energy  $E_{\text{GS},3}^{\text{BO}}$ , obtained in the BOA.

quasiprobability distribution for the mode  $b_{|\uparrow\uparrow\downarrow\downarrow}^{\perp,1}$  is, with  $\alpha = \alpha_R + i\alpha_I$ ,

$$W(\alpha) = \frac{2}{\pi} \exp(-\bar{w}_+ \alpha_R^2 - \bar{w}_- \alpha_I^2), \quad \bar{w}_\pm = 2 \frac{1 \pm w}{1 \mp w}, \quad (13)$$

as derived in the supplemental material [51]. We plot this function for different values of  $\kappa$  in Fig. 2(c,d), to show the increasingly squeezed shape for  $\kappa \searrow \kappa_c$  when approaching the instability. Importantly, although we are close to the critical point,  $\kappa = 0.99\kappa_c$ , where one could expect large ground state displacements because of weak atom confinement, the atoms are in fact on average closer than  $0.4x_0$  to their equilibrium positions (see supplemental material [51]). We note here, that going beyond the considered limit,  $\Omega = 0$ , requires exact numerical diagonalization. This is, however, rather challenging, given that already for such a small system — with all symmetries considered — 9 vibrational modes and 10 electronic states [see Fig. 1(d)] are involved.

*Structural molecular transitions.*—Finally, let us show that this quantum simulation platform permits the investigation of structural molecular transitions and allows to study the impact of quantum effects on those. To this end we consider the triangle shown in Fig. 1(b), which can undergo a transition from a symmetric to a symmetry-broken ground state. Employing the facilitation condition,  $\Delta = -V(d)$ , its resonant electronic subspace is spanned by the states  $\{|\downarrow\uparrow\uparrow\rangle, |\downarrow\uparrow\downarrow\rangle, |\downarrow\uparrow\downarrow\rangle, |\uparrow\downarrow\downarrow\rangle, |\uparrow\downarrow\downarrow\rangle\}$ . The resulting Hamiltonian has the structure of Eq. (8) with  $b_s^{\perp,2} = 0$  and an adjacency matrix that describes a ring-shaped graph [52]. To see the structural transition it is sufficient to employ the so-called BOA, which amounts to neglecting the kinetic energy of the “nuclei”. The resulting Born-Oppenheimer potential energy surfaces (BOPESs) depend on four collective coordinates (bosonic modes), which we label  $q_i$ ,  $i = 1, 2, 3, 4$  (see supplemental material [51]). To compute the MGSE we minimize the (classical) BOPES  $E_{\text{BO}}(\Omega; \mathbf{q})$ , defined as the smallest eigenvalue of the Hamiltonian for a fixed position  $\mathbf{q} = (q_1, q_2, q_3, q_4)^T$  and Rabi frequency  $\Omega$ . Note, that for  $\Omega = 0$  there are three degenerate ground states [52], one for each non-symmetric triangular shape in the top right of Fig. 3(a). This is the so-called Jahn-Teller effect [52–54]. In the vicinity of the leftmost symmetry-broken triangle, and for  $\Omega = 0$ , the BOPES reads

$$E_{\text{BO}}(0; \mathbf{q}) = \frac{\omega}{2x_0^2} \mathbf{q}^2 + \frac{2\kappa}{x_0} q_{\parallel} + \frac{2\xi}{x_0^2} q_{\parallel}^2 + \frac{\sqrt{2}\nu\kappa}{x_0^2} q_{\perp}^2, \quad (14)$$

where  $q_{\parallel} = (q_1 - q_2)/\sqrt{2}$  and  $q_{\perp} = (q_3 + q_4)/\sqrt{2}$ .

Increasing the Rabi frequency leads to a change of the molecular configuration: the distorted triangle becomes a symmetric one [see Fig. 3(a)]. This structural transition is reflected in the ground state energy, which is shown in Fig. 3(b), where we display both the full quantum mechanical result (blue) and the BOA (red). The BOA shows a kink at the transition point, whereas the full numerical calculation yields a smooth curve and is also shifted. These discrepancies are quantum corrections, which are not accounted for by the BOA. The relative shift can be computed analytically for  $\Omega = 0$ ,

$$E_{\text{GS},3} - E_{\text{GS},3}^{\text{BO}} = \frac{\omega}{2} \left[ \sqrt{1 - \xi} + \sqrt{1 - \kappa} - 2 \right], \quad (15)$$

and the explicit calculation (see supplemental material [51]) indeed shows that a non-vanishing commutator between bosonic operators is its origin. The observed smoothed transition is a consequence of the fact that in the vicinity of the transition it is not sufficient to merely consider the minima of the BOA to compute the ground state energy. In fact, here the formerly neglected kinetic energy leads to tunneling between the minima and a gradual and smooth change of the ground state energy.

*Summary and conclusions.*—Optical tweezer arrays in conjunction with Rydberg excitations offer new opportunities for engineering many-body systems that share

central features of complex molecules. Already the simple examples discussed in this work showcase a whole host of interesting phenomena. The quantum simulation toolbox can be further enhanced by introducing resonant (and orientation-dependent) dipolar interactions, which yield a further mechanism — in addition to facilitation — for electronic excitation hopping. This may allow to engineer more complex molecular potential landscapes, for example, conical intersections [11]. Further handles to enrich the quantum simulator are state-dependent and anisotropic tweezer potentials. Ultimately, such a quantum simulator may allow to address fundamental questions concerning dynamical processes in extended molecules. Examples include the impact of vibronic coupling on excitation transfer [55] in light harvesting complexes [56]. Such systems are notoriously difficult to model as the number of phonon degrees of freedom is too large to be exactly simulated [57]. Yet, it is too small to be effectively accounted for through a simple unstructured bath, which would enable a master equation description [58].

*Acknowledgments.*— We acknowledge funding from the Deutsche Forschungsgemeinschaft within the Grant No. 452935230 and the research units FOR5413 (Grant No. 465199066) and FOR5522 (Grant No. 499180199). This work was also supported by the QuantERA II programme (project CoQuaDis, DFG Grant No. 532763411) that has received funding from the EU H2020 research and innovation programme under GA No. 101017733. This work is supported by the ERC grant OPEN-2QS (Grant No. 101164443, <https://doi.org/10.3030/101164443>).

---

[1] L. Pauling, The Nature of the Chemical Bond. Application of Results Obtained from the Quantum Mechanics and from a Theory of Paramagnetic Susceptibility to the Structure of Molecules, *Journal of the American Chemical Society* **53**, 1367 (1931).

[2] C. Lou, Y. Guan, X. Cui, Y. Li, X. Zhou, Q. Yuan, G. Mei, C. Jiao, K. Huang, X. Hou, L. Cao, W. Ji, D. Novko, H. Petek, and M. Feng, Charge-transfer dipole low-frequency vibronic excitation at single-molecular scale, *Science Advances* **10**, 3470 (2024).

[3] H. Li, F. Lan, Y. Wang, X. Lin, Y. Zhao, Q. Zhen, and D. Chen, Molecular Dynamics Simulation and Experimental Study of Mechanical Properties of Graphene–Cement Composites, *Materials* **17**, 410 (2024).

[4] K. Goossens and H. De Winter, Molecular Dynamics Simulations of Membrane Proteins: An Overview, *Journal of Chemical Information and Modeling* **58**, 2193 (2018).

[5] P. W. Atkins and R. S. Friedman, *Molecular Quantum Mechanics*, 5th ed. (Oxford University Press Inc., 2011).

[6] M. Born and R. Oppenheimer, Zur Quantentheorie der Moleküle, *Annalen der Physik* **389**, 457 (1927).

[7] R. W. Schoenlein, L. A. Peteanu, R. A. Mathies, and C. V. Shank, The First Step in Vision: Femtosecond Isomerization of Rhodopsin, *Science* **254**, 412 (1991).

[8] S. Rinaldi, F. Melaccio, S. Gozem, F. Fanelli, and M. Olivucci, Comparison of the isomerization mechanisms of human melanopsin and invertebrate and vertebrate rhodopsins, *Proceedings of the National Academy of Sciences* **111**, 1714 (2014).

[9] Y. I. Manin, *Vychislomoe I Nevychislomoe* (Sov. Radio., 1980) pp. 13–15.

[10] R. P. Feynman, Simulating Physics with Computers, *International Journal of Theoretical Physics* **21**, 467 (1982).

[11] F. M. Gambetta, C. Zhang, M. Hennrich, I. Lesanovsky, and W. Li, Exploring the Many-Body Dynamics Near a Conical Intersection with Trapped Rydberg Ions, *Physical Review Letters* **126**, 233404 (2021).

[12] J. Whitlow, Z. Jia, Y. Wang, C. Fang, J. Kim, and K. R. Brown, Quantum simulation of conical intersections using trapped ions, *Nature Chemistry* **15**, 1509 (2023).

[13] C. H. Valahu, V. C. Olaya-Agudelo, R. J. MacDonell, T. Navickas, A. D. Rao, M. J. Millican, J. B. Pérez-Sánchez, J. Yuen-Zhou, M. J. Biercuk, C. Hempel, T. R. Tan, and I. Kassal, Direct observation of geometric-phase interference in dynamics around a conical intersection, *Nature Chemistry* **15**, 1503 (2023).

[14] C. Boisseau, I. Simbotin, and R. Côté, Macrodimers: Ultralong Range Rydberg Molecules, *Physical Review Letters* **88**, 133004 (2002).

[15] K. R. Overstreet, A. Schwettmann, J. Tallant, D. Booth, and J. P. Shaffer, Observation of electric-field-induced Cs Rydberg atom macrodimers, *Nature Physics* **5**, 581 (2009).

[16] V. Bendkowsky, B. Butscher, J. Nipper, J. P. Shaffer, R. Löw, and T. Pfau, Observation of ultralong-range Rydberg molecules, *Nature* **458**, 7241 (2009).

[17] M. Kiffner, H. Park, W. Li, and T. F. Gallagher, Dipole-dipole-coupled double-Rydberg molecules, *Physical Review A* **86**, 031401 (2012).

[18] H. Saßmannshausen and J. Deiglmayr, Observation of Rydberg-Atom Macrodimers: Micrometer-Sized Diatomic Molecules, *Physical Review Letters* **117**, 083401 (2016).

[19] J. P. Shaffer, S. T. Rittenhouse, and H. R. Sadeghpour, Ultracold Rydberg molecules, *Nature Communications* **9**, 1965 (2018).

[20] M. Exner, R. Srikumar, R. Blättner, M. T. Eiles, P. Schmelcher, and H. Ott, High Precision Spectroscopy of Trilobite Rydberg Molecules, *Physical Review Letters* **134**, 223401 (2025).

[21] S. Wüster and J.-M. Rost, Rydberg aggregates, *Journal of Physics B: Atomic, Molecular and Optical Physics* **51**, 032001 (2018).

[22] H. Schempf, G. Günter, M. Robert-de-Saint-Vincent, C. S. Hofmann, D. Breyel, A. Komnik, D. W. Schönleber, M. Gärttner, J. Evers, S. Whitlock, and M. Weidemüller, Full Counting Statistics of Laser Excited Rydberg Aggregates in a One-Dimensional Geometry, *Physical Review Letters* **112**, 013002 (2014).

[23] R. Faoro, C. Simonelli, M. Archimi, G. Masella, M. M. Valado, E. Arimondo, R. Mannella, D. Ciampini, and O. Morsch, van der Waals explosion of cold Rydberg clusters, *Physical Review A* **93**, 030701 (2016).

[24] Z. Vager, R. Naaman, and E. P. Kanter, Coulomb Explosion Imaging of Small Molecules, *Science* **244**, 426 (1989).

[25] K.-N. Schymik, V. Lienhard, D. Barredo, P. Scholl,

H. Williams, A. Browaeys, and T. Lahaye, Enhanced atom-by-atom assembly of arbitrary tweezer arrays, *Physical Review A* **102**, 063107 (2020).

[26] M. Endres, H. Bernien, A. Keesling, H. Levine, E. R. Anschuetz, A. Krajenbrink, C. Senko, V. Vuletic, M. Greiner, and M. D. Lukin, Atom-by-atom assembly of defect-free one-dimensional cold atom arrays, *Science* **354**, 1024 (2016).

[27] D. Barredo, S. de Léséleuc, V. Lienhard, T. Lahaye, and A. Browaeys, An atom-by-atom assembler of defect-free arbitrary two-dimensional atomic arrays, *Science* **354**, 1021 (2016).

[28] D. Barredo, V. Lienhard, S. de Léséleuc, T. Lahaye, and A. Browaeys, Synthetic three-dimensional atomic structures assembled atom by atom, *Nature* **561**, 79 (2018).

[29] M. Schlosser, S. Tichelmann, D. Schäffner, D. O. de Mello, M. Hambach, J. Schütz, and G. Birk, Scalable Multilayer Architecture of Assembled Single-Atom Qubit Arrays in a Three-Dimensional Talbot Tweezer Lattice, *Physical Review Letters* **130**, 180601 (2023).

[30] L. Ahlheit, C. Nill, D. Svirskiy, J. de Haan, S. Schroers, W. Alt, N. Stiesdal, I. Lesanovsky, and S. Hofferberth, Magic running- and standing-wave optical traps for Rydberg atoms, *Physical Review A* **111**, 013115 (2025).

[31] S. Zhang, F. Robicheaux, and M. Saffman, Magic-wavelength optical traps for Rydberg atoms, *Physical Review A* **84**, 043408 (2011).

[32] M. Saffman, T. G. Walker, and K. Mølmer, Quantum information with Rydberg atoms, *Reviews of Modern Physics* **82**, 2313 (2010).

[33] N. Šibalić, J. D. Pritchard, C. S. Adams, and K. J. Weatherill, ARC: An open-source library for calculating properties of alkali Rydberg atoms, *Computer Physics Communications* **220**, 319 (2017).

[34] K. Singer, J. Stanojevic, M. Weidmüller, and R. Côté, Long-range interactions between alkali Rydberg atom pairs correlated to the  $ns$ - $ns$ ,  $np$ - $np$  and  $nd$ - $nd$  asymptotes, *Journal of Physics B: Atomic, Molecular and Optical Physics* **38**, S295 (2005).

[35] A. Paris-Mandoki, H. Gorniaczyk, C. Tresp, I. Mirgorodskiy, and S. Hofferberth, Tailoring Rydberg interactions via Förster resonances: state combinations, hopping and angular dependence, *Journal of Physics B: Atomic, Molecular and Optical Physics* **49**, 164001 (2016).

[36] D. Petrosyan and K. Mølmer, Binding Potentials and Interaction Gates between Microwave-Dressed Rydberg Atoms, *Physical Review Letters* **113**, 123003 (2014).

[37] T. Förster, Zwischenmolekulare Energiewanderung und Fluoreszenz, *Annalen der Physik* **437**, 55 (1948).

[38] H. Labuhn, S. Ravets, D. Barredo, L. Béguin, F. Nogrette, T. Lahaye, and A. Browaeys, Single-atom addressing in microtraps for quantum-state engineering using Rydberg atoms, *Physical Review A* **90**, 023415 (2014).

[39] A. Browaeys and T. Lahaye, Many-body physics with individually controlled Rydberg atoms, *Nature Physics* **16**, 132 (2020).

[40] F. Nogrette, H. Labuhn, S. Ravets, D. Barredo, L. Béguin, A. Vernier, T. Lahaye, and A. Browaeys, Single-Atom Trapping in Holographic 2D Arrays of Microtraps with Arbitrary Geometries, *Physical Review X* **4**, 021034 (2014).

[41] S.-L. Su, F.-Q. Guo, J.-L. Wu, Z. Jin, X. Q. Shao, and S. Zhang, Rydberg antiblockade regimes: Dynamics and applications, *Europhysics Letters* **131**, 53001 (2020).

[42] C. Ates, T. Pohl, T. Pattard, and J. M. Rost, Antiblockade in Rydberg Excitation of an Ultracold Lattice Gas, *Physical Review Letters* **98**, 023002 (2007).

[43] Y.-Y. Jau, A. M. Hankin, T. Keating, I. H. Deutsch, and G. W. Biedermann, Entangling atomic spins with a Rydberg-dressed spin-flip blockade, *Nature Physics* **12**, 71 (2016).

[44] D. Kurdak, P. R. Banner, Y. Li, S. R. Muleady, A. V. Gorshkov, S. L. Rolston, and J. V. Porto, Enhancement of Rydberg Blockade via Microwave Dressing, *arXiv:2411.08236 [atom-ph]* (2024).

[45] C. Ates, T. Pohl, T. Pattard, and J. M. Rost, Many-body theory of excitation dynamics in an ultracold Rydberg gas, *Physical Review A* **76**, 013413 (2007).

[46] M. Marcuzzi, J. Minář, D. Barredo, S. de Léséleuc, H. Labuhn, T. Lahaye, A. Browaeys, E. Levi, and I. Lesanovsky, Facilitation Dynamics and Localization Phenomena in Rydberg Lattice Gases with Position Disorder, *Physical Review Letters* **118**, 063606 (2017).

[47] D. F. James and J. Jerke, Effective Hamiltonian theory and its applications in quantum information, *Canadian Journal of Physics* **85**, 625–632 (2007).

[48] P. P. Mazza, R. Schmidt, and I. Lesanovsky, Vibrational Dressing in Kinetically Constrained Rydberg Spin Systems, *Physical Review Letters* **125**, 033602 (2020).

[49] M. Magoni, P. P. Mazza, and I. Lesanovsky, Emergent Bloch Oscillations in a Kinetically Constrained Rydberg Spin Lattice, *Physical Review Letters* **126**, 103002 (2021).

[50] D. Brady and M. Fleischhauer, Non-Classical Spin-Phonon Correlations Induced by Rydberg Facilitation in a Lattice, *arXiv:2504.19679 [cond-mat.quant-gas]* (2025).

[51] Supplemental Material: Derivation of analytical results from the main text and numerical procedure for the Born-Oppenheimer approximation.

[52] M. Magoni, R. Joshi, and I. Lesanovsky, Molecular Dynamics in Rydberg Tweezer Arrays: Spin-Phonon Entanglement and Jahn-Teller Effect, *Physical Review Letters* **131**, 093002 (2023).

[53] H. A. Jahn and E. Teller, Stability of Polyatomic Molecules in Degenerate Electronic States. I—Orbital Degeneracy, *Proceedings of the Royal Society A* **161**, 220 (1937).

[54] H. A. Jahn, Stability of Polyatomic Molecules in Degenerate Electronic States. II—Spin Degeneracy, *Proceedings of the Royal Society A* **164**, 117 (1938).

[55] S. Banerjee, A. Baiardi, J. Bloino, and V. Barone, Vibronic Effects on Rates of Excitation Energy Transfer and Their Temperature Dependence, *Journal of Chemical Theory and Computation* **12**, 2357 (2016).

[56] E. A. Arsenault, Y. Yoneda, M. Iwai, K. K. Niyogi, and G. R. Fleming, Vibronic mixing enables ultrafast energy flow in light-harvesting complex II, *Nature Communications* **11**, 1460 (2020).

[57] E. Betti, S. Saraceno, E. Cignoni, L. Cupellini, and B. Mennucci, Insights into Energy Transfer in Light-Harvesting Complex II Through Machine-Learning Assisted Simulations, *The Journal of Physical Chemistry B* **128**, 5188 (2024).

[58] A. Eisfeld and J. S. Briggs, Classical master equation for excitonic transport under the influence of an environment, *Physical Review E* **85**, 046118 (2012).

## SUPPLEMENTAL MATERIAL

### Rydberg atom arrays as quantum simulators for molecular dynamics

Simon Euchner<sup>1</sup> and Igor Lesanovsky<sup>1,2</sup>

<sup>1</sup>*Institut für Theoretische Physik and Center for Integrated Quantum Science and Technology, Universität Tübingen,  
Auf der Morgenstelle 14, 72076 Tübingen, Germany*

<sup>2</sup>*School of Physics and Astronomy and Centre for the Mathematics and Theoretical Physics of Quantum  
Non-Equilibrium Systems, The University of Nottingham, Nottingham, NG7 2RD, United Kingdom*

Here we present some details on results from the main text. In the first section we define the annihilation operators in Eq. (9) from the main text. In the second section we derive the Bogoliubov transformation (BT), give the critical vibronic coupling strengths, and illustrate how the BT is made use of for calculating the molecular ground state energy (MGSE) in the limit  $\Omega = 0$ . In the third section we calculate the Wigner quasiprobability distribution, which is Eq. (13) from the main text. In the fourth section we calculate the ground state atom displacements for the tetrahedron in the limit  $\Omega = 0$ . Finally, in the fifth section, we derive the quantum corrections, Eq. (15), from the main text. Further, the steps involved to generate Fig. 3 from the main text are outlined.

#### Parallel and perpendicular annihilation operators for the tetrahedron

Here we give explicit expressions for the annihilation operators in Eq. (9) from the main text. To do so, we first define the new vector of annihilation operators  $\mathbf{b} = R^T \mathbf{a}$ ,

$$R = \begin{bmatrix} \frac{1}{\sqrt{6}} & 0 & -\frac{1}{2\sqrt{3}} & -\frac{1}{2\sqrt{6}} & -\frac{1}{2\sqrt{3}} & \frac{1}{\sqrt{6}} & -\frac{1}{2\sqrt{2}} & -\frac{1}{2\sqrt{3}} & 0 & \frac{1}{2} & 0 & 0 \\ -\frac{1}{3\sqrt{2}} & -\frac{1}{2\sqrt{6}} & -\frac{1}{6} & -\frac{\sqrt{2}}{3} & \frac{1}{6} & \frac{1}{6\sqrt{2}} & \frac{1}{\sqrt{6}} & -\frac{1}{3} & -\frac{1}{2\sqrt{3}} & 0 & \frac{1}{2} & 0 \\ -\frac{1}{6} & \frac{1}{2\sqrt{3}} & -\frac{\sqrt{2}}{3} & \frac{1}{6} & -\frac{1}{3\sqrt{2}} & -\frac{1}{6} & \frac{1}{2\sqrt{3}} & -\frac{1}{3\sqrt{2}} & \frac{1}{\sqrt{6}} & 0 & 0 & \frac{1}{2} \\ -\frac{1}{\sqrt{6}} & 0 & -\frac{1}{2\sqrt{3}} & -\frac{1}{2\sqrt{6}} & \frac{1}{2\sqrt{3}} & -\frac{1}{\sqrt{6}} & -\frac{1}{2\sqrt{2}} & \frac{1}{2\sqrt{3}} & 0 & \frac{1}{2} & 0 & 0 \\ -\frac{1}{3\sqrt{2}} & -\frac{1}{2\sqrt{6}} & \frac{1}{6} & \frac{\sqrt{2}}{3} & \frac{1}{6} & \frac{1}{6\sqrt{2}} & -\frac{1}{\sqrt{6}} & -\frac{1}{3} & \frac{1}{2\sqrt{3}} & 0 & \frac{1}{2} & 0 \\ -\frac{1}{6} & \frac{1}{2\sqrt{3}} & \frac{\sqrt{2}}{3} & -\frac{1}{6} & -\frac{1}{3\sqrt{2}} & -\frac{1}{6} & -\frac{1}{2\sqrt{3}} & -\frac{1}{3\sqrt{2}} & -\frac{1}{\sqrt{6}} & 0 & 0 & \frac{1}{2} \\ 0 & 0 & 0 & \frac{\sqrt{6}}{4} & 0 & 0 & \frac{1}{2\sqrt{2}} & 0 & -\frac{1}{2} & \frac{1}{2} & 0 & 0 \\ \frac{\sqrt{2}}{3} & -\frac{1}{2\sqrt{6}} & 0 & 0 & -\frac{1}{3} & -\frac{5}{6\sqrt{2}} & 0 & \frac{1}{6} & 0 & 0 & 0 & \frac{1}{2} \\ -\frac{1}{6} & -\frac{1}{\sqrt{3}} & 0 & 0 & -\frac{1}{3\sqrt{2}} & \frac{1}{3} & 0 & \frac{\sqrt{2}}{3} & 0 & 0 & 0 & \frac{1}{2} \\ 0 & 0 & \frac{1}{\sqrt{3}} & -\frac{1}{2\sqrt{6}} & 0 & 0 & \frac{1}{2\sqrt{2}} & 0 & \frac{1}{2} & \frac{1}{2} & 0 & 0 \\ 0 & \frac{\sqrt{6}}{4} & 0 & 0 & 0 & \frac{1}{2\sqrt{2}} & 0 & \frac{1}{2} & 0 & 0 & 0 & \frac{1}{2} \\ \frac{1}{2} & 0 & 0 & 0 & \frac{1}{\sqrt{2}} & 0 & 0 & 0 & 0 & 0 & 0 & \frac{1}{2} \end{bmatrix}, \quad (S1)$$

with  $\mathbf{a} = (a_x^{(1)}, a_y^{(1)}, a_z^{(1)}, \dots, a_x^{(4)}, a_y^{(4)}, a_z^{(4)})^T$  (transposition only acts on  $\mathbb{R}^{12}$ ). The rotation  $R$  we obtain by diagonalizing the real-symmetric twelve-dimensional matrix

$$K = \begin{bmatrix} K^{(2,1)} + K^{(3,1)} + K^{(4,1)} & -K^{(2,1)} & -K^{(3,1)} & -K^{(4,1)} \\ -K^{(2,1)} & K^{(2,1)} + K^{(3,2)} + K^{(4,2)} & -K^{(3,2)} & -K^{(4,2)} \\ -K^{(3,1)} & -K^{(3,2)} & K^{(3,1)} + K^{(3,2)} + K^{(4,3)} & -K^{(4,3)} \\ -K^{(4,1)} & -K^{(4,2)} & -K^{(4,3)} & K^{(4,1)} + K^{(4,2)} + K^{(4,3)} \end{bmatrix}, \quad (S2)$$

where  $K^{(k,l)} = H_a^{(k,l)} + H_b^{(k,l)}$  [see Eq. (5) and Eq. (6) from the main text]. This matrix is the Hessian of the potential  $U$  that is obtained by setting  $n^{(1)} = \dots = n^{(4)} = 1$  in Eq. (2) from the main text, i.e.,

$$U(\mathbf{r}^{(1)}, \mathbf{r}^{(2)}, \mathbf{r}^{(3)}, \mathbf{r}^{(4)}) = V(r^{(2,1)}) + V(r^{(3,1)}) + V(r^{(3,2)}) + V(r^{(4,1)}) + V(r^{(4,2)}) + V(r^{(4,3)}), \quad (S3)$$

with  $\mathbf{r}^{(k,l)} = \|\mathbf{r}^{(k)} - \mathbf{r}^{(l)}\|$ . The last three columns define  $b_{10}$ ,  $b_{11}$ , and  $b_{12}$ . These three modes describe center-of-mass shifts of the tetrahedron, such that they decouple due to momentum conservation. Hence, this symmetry allows to

reduce the description to  $12 - 3 = 9$  bosonic modes. Generally,  $R$  does not diagonalize the interaction Hamiltonian in Eq. (2) from the main text. This is because, generally, we need to employ an electronic state-dependent rotation to define new annihilation operators such that the Hessian on each electronic subspace is diagonal. This is best illustrated via an example. On the subspace  $|\uparrow\uparrow\downarrow\downarrow\rangle$  the vibronic Hamiltonian is given by the expression

$$h_{|\uparrow\uparrow\downarrow\downarrow\rangle} = \omega \mathbf{a}^\dagger \mathbf{a} + \frac{x_0}{\sqrt{2}} [-\mathbf{G}^{(2,1)}, \mathbf{G}^{(2,1)}, \mathbf{0}^T, \mathbf{0}^T] (\mathbf{a} + (\mathbf{a}^\dagger)^T) + \frac{x_0^2}{4} (\mathbf{a}^\dagger + \mathbf{a}^T) L^{(2,1)} (\mathbf{a} + (\mathbf{a}^\dagger)^T) \quad (\text{S4})$$

$$= \omega \mathbf{b}^\dagger \mathbf{b} + \frac{x_0}{\sqrt{2}} [-\mathbf{G}^{(2,1)}, \mathbf{G}^{(2,1)}, \mathbf{0}^T, \mathbf{0}^T] R (\mathbf{b} + (\mathbf{b}^\dagger)^T) + \frac{x_0^2}{4} (\mathbf{b}^\dagger + \mathbf{b}^T) R^T L^{(2,1)} R (\mathbf{b} + (\mathbf{b}^\dagger)^T). \quad (\text{S5})$$

Here, the vector  $\mathbf{G}^{(2,1)}$  is defined in the main text in Eq. (4) and we introduced the real-symmetric matrix

$$L^{(2,1)} = \begin{bmatrix} K^{(2,1)} & -K^{(2,1)} & 0_3 & 0_3 \\ -K^{(2,1)} & K^{(2,1)} & 0_3 & 0_3 \\ 0_3 & 0_3 & 0_3 & 0_3 \\ 0_3 & 0_3 & 0_3 & 0_3 \end{bmatrix}, \quad (\text{S6})$$

where  $0_3$  is the three-dimensional zero matrix. Generally,  $R^T L^{(2,1)} R$  is not diagonal, such that the modes mix. In fact, it is generally impossible to find a transformation  $R$  such that  $R^T L^{(k,l)} R$  is diagonal for all  $k$  and  $l$ , because the commutators  $[L^{(k,l)}, L^{(k',l')}]$ , generally, do not vanish. In order to cancel mixing of the modes we utilize a state-dependent second rotation  $R_{|\uparrow\uparrow\downarrow\downarrow\rangle}$  for which  $R_{|\uparrow\uparrow\downarrow\downarrow\rangle}^T (R^T L^{(2,1)} R) R_{|\uparrow\uparrow\downarrow\downarrow\rangle}$  is diagonal. With this second rotation we define the state-dependent annihilation operators  $\mathbf{b}_{|\uparrow\uparrow\downarrow\downarrow\rangle} = R_{|\uparrow\uparrow\downarrow\downarrow\rangle}^T \mathbf{b}$ . Using these yields the expression for  $h_{|\uparrow\uparrow\downarrow\downarrow\rangle}$  given in Eq. (9) from the main text. We apply this process for all states  $s$  representing a node in the graph depicted in Fig. 1(d) from the main text, such that we generally define  $\mathbf{b}_s = R_s^T \mathbf{a}$ . If the state  $s$  hosts two Rydberg atoms, we find that there are only three modes which are not described by a free harmonic oscillator. These three modes are the parallel and perpendicular modes from the main text in Eq. (9). Here we give the explicit expressions for the annihilation operators associated to the subspace  $s = |\uparrow\uparrow\downarrow\downarrow\rangle$ :

$$b_{|\uparrow\uparrow\downarrow\downarrow\rangle}^{\parallel} = \frac{1}{\sqrt{2}} (a_x^{(1)} - a_x^{(2)}), \quad b_{|\uparrow\uparrow\downarrow\downarrow\rangle}^{\perp,1} = \frac{1}{\sqrt{2}} (a_y^{(1)} - a_y^{(2)}), \quad b_{|\uparrow\uparrow\downarrow\downarrow\rangle}^{\perp,2} = \frac{1}{\sqrt{2}} (a_z^{(1)} - a_z^{(2)}) \quad (\text{S7})$$

Of course this is not the only possible choice, since the rotations  $R_{|\uparrow\uparrow\downarrow\downarrow\rangle}$  and  $R$  are not unique.

### Bogoliubov transformation, ground state energy, and critical coupling strengths

Here we derive the BT used in the main text, extract the critical coupling strengths  $\xi_c$  and  $\kappa_c$ , and show how the ground state energy of the arrays in Fig. 1(a-c) from the main text can be calculated in the limit  $\Omega = 0$ .

We start with the BT. To this end we consider the generic bosonic Hamiltonian

$$h = \omega b^\dagger b + \lambda(b^\dagger + b) + \gamma(b^\dagger + b)^2, \quad (\text{S8})$$

with  $\omega > 0$  and  $\lambda, \gamma \in \mathbb{R}$ . Appropriate substitutions of the parameters  $\lambda$  and  $\gamma$  yield the perturbed harmonic oscillators in Eq. (7) and Eq. (9) from the main text. Our goal is to find a BT  $b_{\text{BT}} = ub + vb^\dagger$ , with  $u, v \in \mathbb{C}$  such that the quadratic off-diagonal terms vanish. Without loss of generality we choose  $u \geq 0$ . Note that  $b_{\text{BT}}$  obeys bosonic algebra if and only if  $|u|^2 - |v|^2 = 1$ , such that  $u = 0$  is not a solution. Therefore, we do not loose solutions by assuming  $u > 0$ . To obtain equations which fix  $u$  and  $v$  we first substitute the inverse transformation  $b = u^* b_{\text{BT}}^\dagger - v b_{\text{BT}}$  into Eq. (S8). The result is

$$h = ((\omega + 2\gamma)(|u|^2 + |v|^2) - 2\gamma(uv^* + u^*v)) b_{\text{BT}}^\dagger b_{\text{BT}} + \lambda((u - v)b_{\text{BT}}^\dagger + (u^* - v^*)b_{\text{BT}}) + (f(u, v)b_{\text{BT}}^{\dagger 2} + f^*(u, v)b_{\text{BT}}^2) + (\omega + 2\gamma)|v|^2 + \gamma(1 - uv^* - u^*v). \quad (\text{S9})$$

Here we defined the function  $f(u, v) = \gamma(u^2 + v^2) - (\omega + 2\gamma)uv$ . To achieve our goal we choose  $u$  and  $v$  such that  $f(u, v) = 0$ . Since  $u > 0$ , the ratio  $w = v/u$  is well defined and we find that  $f(u, v) = 0$  is equivalent to the condition

$$\gamma w^2 - (\omega + 2\gamma)w + \gamma = 0. \quad (\text{S10})$$

For  $\gamma = 0$ , Eq. (S8) does not host terms like  $b^2$  and  $(b^\dagger)^2$ , such that the BT is trivial. Let now  $\gamma \neq 0$ . Solving for  $w$  yields

$$w = \begin{cases} 1 + \phi \pm \sqrt{(1 + \phi)^2 - 1}, & (1 + \phi)^2 > 1 \\ 1 + \phi \pm i\sqrt{1 - (1 + \phi)^2}, & (1 + \phi)^2 \leq 1 \end{cases}, \quad \phi = \frac{\omega}{2\gamma}. \quad (\text{S11})$$

To obtain the BT we further enforce the condition  $|u|^2 - |v|^2 = 1$ , which turns out to be impossible if  $(1 + \phi)^2 \leq 1$ , since  $|w| = 1$ . In case  $(1 + \phi)^2 > 1$  we always find a solution that obeys  $|w| < 1$ . The condition for solutions to exist can thus be expressed as  $\phi \in (-\infty, -2) \cup (0, \infty)$ . Therefore, we close (again allowing the case  $\gamma = 0$ ) that the BT exists if and only if  $2\gamma/\omega \in (-1/2, \infty)$ . In the regime where a solution for  $u$  and  $v$  exists, we obtain

$$u = \frac{1}{\sqrt{1 - w^2}}, \quad v = \frac{w}{\sqrt{1 - w^2}}, \quad (\text{S12})$$

where

$$w = 1 + \phi - \frac{\phi}{|\phi|} \sqrt{(1 + \phi)^2 - 1}, \quad \phi = \frac{\omega}{2\gamma}, \quad (\text{S13})$$

which is Eq. (10) from the main text.

The condition that determines if the BT exists, yields the critical parameter  $\gamma_c = -\omega/4$ . For  $\gamma = \xi$  [cf. Eq. (7) from the main text] we have  $\xi_c = -\omega/4$ . In the case  $\lambda = 0$  and  $\gamma = \nu\kappa/\sqrt{2}$  we recover the Hamiltonian associated to the annihilation operator  $b_s^{\perp,1}$  [cf. Eq. (9) from the main text]. In this case  $\gamma_c = -\omega/4$  results in  $\nu\kappa_c/\sqrt{2} = -\omega/4$ , i.e., the critical coupling strength  $\kappa_c = -\omega/(2\sqrt{2}\nu)$ .

With the BT at hand it is now straight forward to calculate the MGSE in the limit  $\Omega = 0$  for the arrays in Fig. 1(a-c) from the main text. As an example we illustrate this for the dumbbell. In the limit  $\Omega = 0$  there are two possibilities for the ground state: either  $|+\rangle \otimes |\text{vac}\rangle_b$ , where  $|\text{vac}\rangle_b$  is the vacuum of the annihilation operator  $b$ , or  $|\uparrow\uparrow\rangle \otimes |\text{gs}\rangle$ , with the ground state  $|\text{gs}\rangle$  of the perturbed harmonic oscillator

$$H = \omega b^\dagger b + \sqrt{2}\kappa(b + b^\dagger) + \xi(b + b^\dagger)^2. \quad (\text{S14})$$

If the ground state is  $|+\rangle \otimes |\text{vac}\rangle_b$ , the ground state energy is zero. Therefore, the ground state is given by  $|+\rangle \otimes |\text{vac}\rangle_b$  only if the ground state energy of  $H$  is larger than zero. If the ground state energy of  $H$  is zero, the ground state is twofold-degenerate. Combining all of this results in the expression  $E_{\text{GS},2} = \min\{\omega\varepsilon_s, 0\}$  for the MGSE, where  $\omega\varepsilon_2$  is the ground state energy of  $H$ . To determine  $\varepsilon_2$  we first apply the BT to  $H$ , which leads to

$$H = \omega\sqrt{1 - \bar{\xi}}b_{\text{BT}}^\dagger b_{\text{BT}} + \frac{\sqrt{2}\kappa}{(1 - \bar{\xi})^{1/4}}(b_{\text{BT}} + b_{\text{BT}}^\dagger) + \frac{\omega}{2}\sqrt{1 - \bar{\xi}} - \frac{\omega}{2}, \quad \bar{\xi} = \frac{\xi}{\xi_c}. \quad (\text{S15})$$

Next, we transform into a displaced frame of reference using the displacement operator

$$D(b_{\text{BT}}, \mu) = \exp\left(\mu b_{\text{BT}}^\dagger - \mu^* b_{\text{BT}}\right), \quad \mu = -\frac{\sqrt{2}\kappa}{\omega} \frac{1}{(1 - \bar{\xi})^{3/4}}. \quad (\text{S16})$$

In the displaced frame we find

$$D^\dagger(b_{\text{BT}}, \mu)H D(b_{\text{BT}}, \mu) = \omega\sqrt{1 - \bar{\xi}}b_{\text{BT}}^\dagger b_{\text{BT}} - \frac{2\kappa^2}{\omega} \frac{1}{1 - \bar{\xi}} + \frac{\omega}{2}\sqrt{1 - \bar{\xi}} - \frac{\omega}{2}. \quad (\text{S17})$$

Clearly, the ground state of the displaced Hamiltonian is the vacuum of  $b_{\text{BT}}$ , such that we identify  $\omega\varepsilon_2$  to be the additive constant to the free harmonic oscillator, which is Eq. (11) from the main text. Analogously, we find  $\varepsilon_4$  in Eq. (12) from the main text.

### Wigner quasiprobability distribution

In this section we derive the Wigner quasiprobability distribution that is given in Eq. (13) from the main text. This means that we calculate it for the pure state  $\rho_{\text{gs}} = |\text{gs}\rangle\langle\text{gs}|$  and the annihilation operator  $c = b_{|\uparrow\uparrow\downarrow\downarrow\rangle}^{\perp,1}$ . Here,  $|\text{gs}\rangle$  is the ground state of the Hamiltonian [see Eq. (9) from the main text] associated to the annihilation operator  $c$ , i.e.,

$$H = \omega c^\dagger c + \frac{\nu\kappa}{\sqrt{2}}(c + c^\dagger)^2. \quad (\text{S18})$$

Note that the state  $|GS\rangle$  from the main text is not equal to  $|gs\rangle$ , because  $|GS\rangle$  is the ground state of  $h_{|\uparrow\uparrow\downarrow\downarrow\rangle}$ , not just the ground state of  $H$ . The first step now is to calculate  $|gs\rangle$ . To this end we rewrite it in terms of the new annihilation operator  $c_{\text{BT}} = (c + wc^\dagger)/\sqrt{1 - w^2}$ , where  $w$  is given by Eq. (S13) with the substitution  $\gamma = \nu\kappa/\sqrt{2}$ . Making use of Eq. (S9), we arrive at

$$H = \omega\sqrt{1 - \bar{\kappa}}c_{\text{BT}}^\dagger c_{\text{BT}} + \frac{\omega}{2}\sqrt{1 - \bar{\kappa}} - \frac{\omega}{2}, \quad \bar{\kappa} = \frac{\kappa}{\kappa_c}. \quad (\text{S19})$$

From this expression we close that the ground state is given by the vacuum of  $c_{\text{BT}}$ , i.e.  $|gs\rangle = |\text{vac}\rangle_{c_{\text{BT}}}$ . To relate this state to Fock states associated to the annihilation operator  $c$ , we use that the BT acts on the Hilbert space in the form of a squeezing operator:

$$c_{\text{BT}} = S^\dagger(c, \sigma)cS(c, \sigma), \quad S(c, \sigma) = \exp\left(\frac{\sigma^*}{2}c^2 - \frac{\sigma}{2}(c^\dagger)^2\right) \quad (\text{S20})$$

In our case,  $\sigma = -\text{artanh}(w)$ , with  $w$  given by Eq. (S13) for  $\gamma = \nu\kappa/\sqrt{2}$ . Note that this is well defined because  $|w| < 1$  if the BT exists. Since by definition the ground state is annihilated by  $c$ ,

$$0 = S^\dagger(c, \sigma)c|\text{vac}\rangle_c = S^\dagger(c, \sigma)S(c, \sigma)c_{\text{BT}}S^\dagger(c, \sigma)|\text{vac}\rangle_c = c_{\text{BT}}S^\dagger(c, \sigma)|\text{vac}\rangle_c. \quad (\text{S21})$$

Up to a phase, this yields the relation  $|\text{vac}\rangle_{c_{\text{BT}}} = S^\dagger(c, \sigma)|\text{vac}\rangle_c$ . Therefore, in the ground state  $\rho_{\text{gs}}$ , we find that the expectation value of the displacement operator [defined in Eq. (S16)]

$$D(c, \beta) = \exp(\beta c^\dagger - \beta^* c) \quad (\text{S22})$$

acquires the form

$$f(\beta) = \text{tr}(\rho_{\text{gs}}D(c, \beta)) = \exp\left(-\frac{1}{2}\frac{|\beta + w\beta^*|}{1 - w^2}\right), \quad (\text{S23})$$

with  $\beta \in \mathbb{C}$ . Finally, to obtain the Wigner quasiprobability distribution  $W$ , we essentially take the complex Fourier transformation of  $f$ :

$$W(\alpha) = \frac{1}{\pi^2} \int_{\mathbb{C}} d\beta f(\beta) e^{\beta^* \alpha - \alpha^* \beta} \quad (\text{S24})$$

The integration results in Eq. (13) from the main text.

### Ground state displacements at vanishing Rabi frequency

In this section we justify the claim that in the state  $|\uparrow\uparrow\downarrow\downarrow\rangle \otimes |GS\rangle$ , that is used to calculate the Wigner quasiprobability distribution, the atoms are displaced less than  $0.4x_0$  from their equilibrium position, for the vibronic couplings given in the caption of Fig. 2(c,d) and  $\kappa = 0.99\kappa_c$ . To this end, we derive an analytical expression for the ground state displacements in this state. The first step is to obtain  $|GS\rangle$ , which is the ground state of the Hamiltonian [see Eq. (9) in the main text]

$$h_{|\uparrow\uparrow\downarrow\downarrow\rangle} = \omega b_{|\uparrow\uparrow\downarrow\downarrow\rangle}^\dagger b_{|\uparrow\uparrow\downarrow\downarrow\rangle} + \sqrt{2}\kappa(b_{|\uparrow\uparrow\downarrow\downarrow\rangle}^{\parallel} + (b_{|\uparrow\uparrow\downarrow\downarrow\rangle}^{\parallel})^\dagger) + \xi(b_{|\uparrow\uparrow\downarrow\downarrow\rangle}^{\parallel} + (b_{|\uparrow\uparrow\downarrow\downarrow\rangle}^{\parallel})^\dagger)^2 + \frac{\nu\kappa}{\sqrt{2}}(b_{|\uparrow\uparrow\downarrow\downarrow\rangle}^{\perp,1} + (b_{|\uparrow\uparrow\downarrow\downarrow\rangle}^{\perp,1})^\dagger)^2 + \frac{\nu\kappa}{\sqrt{2}}(b_{|\uparrow\uparrow\downarrow\downarrow\rangle}^{\perp,2} + (b_{|\uparrow\uparrow\downarrow\downarrow\rangle}^{\perp,2})^\dagger)^2. \quad (\text{S25})$$

The ground state of the modes which are described by free harmonic oscillators is the vacuum, such that they do not yield finite displacements. Next, we observe that the ground state associated to the perpendicular modes is a squeezed vacuum, because there are no linear contributions in  $b_{|\uparrow\uparrow\downarrow\downarrow\rangle}^{\perp,j}$ . Therefore,  $\langle GS|(b_s^{\perp,j} + (b_s^{\perp,j})^\dagger)|GS\rangle = 0$ . From this we close that only  $b_{|\uparrow\uparrow\downarrow\downarrow\rangle}^{\parallel}$  yields finite displacements. Calculating them amounts to evaluating the expectation value

$$\frac{\delta}{x_0} = \frac{1}{\sqrt{2}} \langle \text{gs}|b_{|\uparrow\uparrow\downarrow\downarrow\rangle}^{\parallel} + (b_{|\uparrow\uparrow\downarrow\downarrow\rangle}^{\parallel})^\dagger|\text{gs}\rangle, \quad (\text{S26})$$

where  $|\text{gs}\rangle$  is the ground state of the single-mode Hamiltonian

$$H = \omega c^\dagger c + \sqrt{2}\kappa(c + c^\dagger) + \xi(c + c^\dagger)^2, \quad c \equiv b_{|\uparrow\uparrow\downarrow\downarrow\rangle}^\dagger. \quad (\text{S27})$$

We note that this is the same expression as in Eq. (S14). Hence, we find

$$D^\dagger(c_{\text{BT}}, \mu) H D(c_{\text{BT}}, \mu) = \omega \sqrt{1 - \xi} c_{\text{BT}}^\dagger c_{\text{BT}} - \frac{2\kappa^2}{\omega} \frac{1}{1 - \xi} + \frac{\omega}{2} \sqrt{1 - \xi} - \frac{\omega}{2}, \quad (\text{S28})$$

with the displacement operator  $D(c_{\text{BT}}, \mu)$  defined in Eq. (S16). The ground state in this frame is the vacuum,  $|\text{vac}\rangle_{c_{\text{BT}}}$ , of the annihilation operator  $c_{\text{BT}}$ . Transforming back into the non-displaced frame yields the ground state

$$|\text{gs}\rangle = D(c_{\text{BT}}, \mu) S^\dagger(c, \sigma) |\text{vac}\rangle_c = D(S^\dagger(c, \sigma) c S(c, \sigma), \mu) S^\dagger(c, \sigma) |\text{vac}\rangle_c = S^\dagger(c, \sigma) D(c, \mu) |\text{vac}\rangle_c, \quad (\text{S29})$$

with the squeezing operator [cf. Eq. (S20)]  $S(c, \sigma)$  associated to  $c$  and  $\sigma = -\text{artanh}(w)$ , where  $w$  is given by Eq. (S13) after the substitution  $\gamma = \xi$ . Employing this expression, we calculate

$$\frac{\delta}{x_0} = \frac{1}{\sqrt{2}} \langle \text{vac} |_c D^\dagger(c, \mu) S(c, \sigma) (c + c^\dagger) S^\dagger(c, \sigma) D(c, \mu) |\text{vac}\rangle_c = \frac{1}{\sqrt{2}} \langle \mu |_c S(c, \sigma) (c + c^\dagger) S^\dagger(c, \sigma) |\mu\rangle_c, \quad (\text{S30})$$

where  $|\mu\rangle_c$  denotes a coherent state of amplitude  $\mu$  with respect to  $c$ . Next, we combine  $S^\dagger(\sigma, b) = S(-\sigma, b)$ , Eq. (S20), and Eq. (S12) to arrive at

$$\frac{\delta}{x_0} = \frac{1}{\sqrt{2}} \langle \text{gs} | (c + c^\dagger) |\text{gs}\rangle = \frac{1}{\sqrt{2}} \sqrt{\frac{1-w}{1+w}} \langle \mu |_c (c + c^\dagger) |\mu\rangle_c = \frac{1}{\sqrt{2}} \sqrt{\frac{1-w}{1+w}} (\mu + \mu^*). \quad (\text{S31})$$

Finally, plugging in the explicit expressions for  $\mu$  [see Eq. (S16)] and  $w$  [see Eq. (S13) with  $\gamma = \xi$ ] results in

$$\frac{\delta}{x_0} = -\frac{2\kappa}{\omega} \frac{1}{1 - \xi}. \quad (\text{S32})$$

Note that because of symmetry, on average, each of the two Rydberg atoms associated to the state  $|\uparrow\uparrow\downarrow\downarrow\rangle$  is displaced  $|\delta|/2$  from its equilibrium position. For the vibronic couplings  $\kappa = 0.99\kappa_c$ ,  $\xi = 2.0\omega$ , and  $\nu = 0.10$  [see caption of Fig. 2(c,d)] we obtain  $|\delta|/2 \approx 0.39x_0 < 0.40x_0$ , which is the value given in the main text.

### Born-Oppenheimer approximation for the triangle

This final section's purpose is twofold: first, we derive Eq. (15) from the main text, showing that, indeed, this contribution is the consequence of the non-vanishing bosonic commutators, and secondly, we want to outline the numerical procedure which we apply to produce Fig. 3 from the main text.

To obtain Eq. (15) from the main text, we need the exact expression,  $E_{\text{GS},3}$ , for the MGSE as well as the result in the Born-Oppenheimer approximation (BOA),  $E_{\text{GS},3}^{\text{BO}}$ . We first calculate the exact result. To this end, analogously to the tetrahedron, we define the annihilation operators  $\mathbf{b} = R^T \mathbf{a}$ ,

$$R = \begin{bmatrix} \frac{1}{2} & -\frac{1}{2} & \frac{1}{2\sqrt{3}} & -\frac{1}{2\sqrt{3}} & \frac{1}{\sqrt{3}} & 0 \\ -\frac{1}{2\sqrt{3}} & -\frac{1}{2\sqrt{3}} & -\frac{1}{2} & -\frac{1}{2} & 0 & \frac{1}{\sqrt{3}} \\ -\frac{1}{2} & \frac{1}{2} & \frac{1}{2\sqrt{3}} & -\frac{1}{2\sqrt{3}} & \frac{1}{\sqrt{3}} & 0 \\ -\frac{1}{2\sqrt{3}} & -\frac{1}{2\sqrt{3}} & \frac{1}{2} & \frac{1}{2} & 0 & \frac{1}{\sqrt{3}} \\ 0 & 0 & -\frac{1}{\sqrt{3}} & \frac{1}{\sqrt{3}} & \frac{1}{\sqrt{3}} & 0 \\ \frac{1}{\sqrt{3}} & \frac{1}{\sqrt{3}} & 0 & 0 & 0 & \frac{1}{\sqrt{3}} \end{bmatrix}. \quad (\text{S33})$$

The rotation  $R$  diagonalizes the six-dimensional matrix

$$K = \begin{bmatrix} K^{(2,1)} + K^{(3,1)} & -K^{(2,1)} & -K^{(3,1)} \\ -K^{(2,1)} & K^{(2,1)} + K^{(3,2)} & -K^{(3,2)} \\ -K^{(3,1)} & -K^{(3,2)} & K^{(3,1)} + K^{(3,2)} \end{bmatrix}. \quad (\text{S34})$$

Here we defined the vector of annihilation operators  $\mathbf{a} = (a_x^{(1)}, a_y^{(1)}, a_x^{(2)}, a_y^{(2)}, a_x^{(3)}, a_y^{(3)})^T$ , where transposition acts solely on  $\mathbb{R}^6$ . The modes associated to  $b_5$  and  $b_6$  decouple because of momentum conservation, such that only four modes remain as a consequence of this symmetry. To obtain the MGSE in the limit  $\Omega = 0$  we note that the Hamiltonian for the triangle has the same form as Eq. (8) from the main text. The ground state is three-fold degenerate. Depending on the vibronic couplings  $\kappa$ ,  $\xi$ , and  $\nu$ , the eigenspace associated to the MGSE is either spanned by

$$|\uparrow\downarrow\downarrow\rangle \otimes |\text{vac}\rangle_{\mathbf{b}}, \quad |\downarrow\uparrow\downarrow\rangle \otimes |\text{vac}\rangle_{\mathbf{b}}, \quad |\downarrow\downarrow\uparrow\rangle \otimes |\text{vac}\rangle_{\mathbf{b}}. \quad (\text{S35})$$

or

$$|\uparrow\uparrow\downarrow\rangle \otimes |gs\rangle_{\uparrow\uparrow\downarrow}, \quad |\downarrow\uparrow\uparrow\rangle \otimes |gs\rangle_{\downarrow\uparrow\uparrow}, \quad |\uparrow\downarrow\uparrow\rangle \otimes |gs\rangle_{\uparrow\downarrow\uparrow}, \quad (S36)$$

where  $|\text{vac}\rangle_b$  is the multimode vacuum of the annihilation operators  $\mathbf{b}$  and  $|gs\rangle_s$  is the ground state of the Hamiltonian  $h_s$  [cf. Eq. (8) from the main text]. As an example, for  $s = |\uparrow\uparrow\downarrow\rangle$ , the vibronic Hamiltonian is

$$h_{|\uparrow\uparrow\downarrow\rangle} = \omega \mathbf{b}^\dagger \mathbf{b} + \sqrt{2}\kappa(b_{|\uparrow\uparrow\downarrow\rangle}^{\parallel} + (b_{|\uparrow\uparrow\downarrow\rangle}^{\parallel})^\dagger) + \xi(b_{|\uparrow\uparrow\downarrow\rangle}^{\parallel} + (b_{|\uparrow\uparrow\downarrow\rangle}^{\parallel})^\dagger)^2 + \frac{\nu\kappa}{\sqrt{2}}(b_{|\uparrow\uparrow\downarrow\rangle}^{\perp} + (b_{|\uparrow\uparrow\downarrow\rangle}^{\perp})^\dagger)^2, \quad (S37)$$

where

$$b_{|\uparrow\uparrow\downarrow\rangle}^{\parallel} = \frac{1}{\sqrt{2}}(b_1 - b_2) = \frac{1}{\sqrt{2}}(a_x^{(1)} - a_x^{(2)}), \quad b_{|\uparrow\uparrow\downarrow\rangle}^{\perp} = \frac{1}{\sqrt{2}}(b_3 + b_4) = -\frac{1}{\sqrt{2}}(a_y^{(1)} - a_y^{(2)}). \quad (S38)$$

If the ground state is a linear combination of the states in Eq. (S35), the MGSE is zero. Hence, we close that the ground state is a linear combination of the states in Eq. (S36) only if the ground state energy,  $\omega\varepsilon_3$ , of  $h_{|\uparrow\uparrow\downarrow\rangle}$  is less than zero. We summarize this discussion in the expression  $E_{\text{GS},3} = \min\{\omega\varepsilon_3, 0\}$  for the MGSE. What is left to do now is to find an expression for  $\omega\varepsilon_3$ . To this end we diagonalize Eq. (S37), which we achieve by employing the BT defined by Eq. (S12) and Eq. (S13). We apply this transformation to the Hamiltonians associated to the parallel,  $b_{|\uparrow\uparrow\downarrow\rangle}^{\parallel}$ , and perpendicular,  $b_{|\uparrow\uparrow\downarrow\rangle}^{\perp}$ , annihilation operator, separately. Both of the resulting single-mode Hamiltonians are analogous to Eq. (S14), such that we directly obtain

$$\varepsilon_3 = -\frac{2\kappa^2}{\omega^2} \frac{1}{1-\xi} + \frac{1}{2} \sqrt{1-\xi} + \frac{1}{2} \sqrt{1-\bar{\kappa}} - 1. \quad (S39)$$

Apart from the first one, all of these terms can be traced back to

$$(\omega + 2\gamma)|v|^2 + \gamma(1 - uv^* - u^*v) \quad (S40)$$

in Eq. (S9). Importantly, this contribution results from the non-vanishing commutators of the bosonic algebra. The next step is to calculate the MGSE in the BOA. To this end we express the full Hamiltonian in the quadratures  $q_i = x_0(b_i + b_i^\dagger)/\sqrt{2}$ ,  $i = 1, 2, 3, 4$  ( $b_5$  and  $b_6$  are decoupled because of momentum conservation), and their conjugated momenta  $p_i$ . We collect the positions and momenta in the vectors  $\mathbf{q}$  and  $\mathbf{p}$ . Expressed in them, the full Hamiltonian acquires the form

$$\begin{aligned} H_3 = & \Omega \sum_{ss'} B_{ss'} |s\rangle\langle s'| + \frac{\omega}{2} \left[ \frac{\mathbf{q}^2}{x_0^2} + x_0^2 \mathbf{p}^2 \right] \\ & + |\uparrow\uparrow\downarrow\rangle\langle\uparrow\uparrow\downarrow| \left[ \frac{\sqrt{2}\kappa}{x_0} (q_1 - q_2) + \frac{\xi}{x_0^2} (q_1 - q_2)^2 + \frac{\nu\kappa}{\sqrt{2}x_0^2} (q_3 + q_4)^2 \right] \\ & + |\downarrow\uparrow\uparrow\rangle\langle\downarrow\uparrow\uparrow| \left[ \frac{\sqrt{2}\kappa}{x_0} \left( q_1 + \frac{1}{2}q_2 - \frac{\sqrt{3}}{2}q_3 \right) + \frac{\xi}{x_0^2} \left( q_1 + \frac{1}{2}q_2 - \frac{\sqrt{3}}{2}q_3 \right)^2 + \frac{\nu\kappa}{\sqrt{2}x_0^2} \left( \frac{\sqrt{3}}{2}q_2 + \frac{1}{2}q_3 - q_4 \right)^2 \right] \\ & + |\uparrow\downarrow\uparrow\rangle\langle\uparrow\downarrow\uparrow| \left[ \frac{\sqrt{2}\kappa}{x_0} \left( q_1 + \frac{1}{2}q_2 + \frac{\sqrt{3}}{2}q_3 \right) + \frac{\xi}{x_0^2} \left( q_1 + \frac{1}{2}q_2 + \frac{\sqrt{3}}{2}q_3 \right)^2 + \frac{\nu\kappa}{\sqrt{2}x_0^2} \left( -\frac{\sqrt{3}}{2}q_2 + \frac{1}{2}q_3 - q_4 \right)^2 \right]. \end{aligned} \quad (S41)$$

Applying the BOA, which amounts to setting  $\mathbf{p} = \mathbf{0}$ , allows to treat  $\mathbf{q}$  classically. Next, we define the ground state potential energy surface as the map  $E_{\text{BO}}$ , which maps a position  $\mathbf{q}$  to the smallest eigenvalue of Eq. (S41) for  $\mathbf{p} = \mathbf{0}$ . The MGSE is then approximated by the minimum value of this surface. In the limit  $\Omega = 0$  we can give an analytical expression for  $E_{\text{BO}}$ , which is Eq. (14) from the main text. Since this is a simple parabola we obtain for the minimum

$$E_{\text{GS},3}^{\text{BO}} = -\frac{2\kappa^2}{\omega} \frac{1}{1-\xi}. \quad (S42)$$

With this expression we recover Eq. (15) from the main text by subtracting Eq. (S42) from Eq. (S39). Note that the vibronic couplings given in the caption of Fig. 3(a) from the main text yield  $E_{\text{GS},3} = \omega\varepsilon_3 < 0$ .

Finally, we outline how Fig. 3 from the main text is generated. First, we fix all vibronic couplings to the values presented in the caption of the figure. With these constants fixed,  $E_{\text{BO}}$  is now a function of  $\Omega$  and  $\mathbf{q}$ . We then use a

standard minimization algorithm to obtain the (approximate) MGSE for a range of  $\Omega$ . The resulting (red) curve is shown in Fig. 3(b) from the main text. To obtain the three curves in Fig. 3(a) from the main text, we first note that in the symmetry-broken regime  $E_{\text{BO}}$  hosts three degenerate global minima, corresponding to the symmetry-broken triangular configurations depicted in the top right (see also [52]). To show the transition we plot  $E_{\text{BO}}$  in the vicinity of the global minimum which is associated with the leftmost symmetry-broken triangle. At this specific minimum  $q_3 = q_4 = 0$ . In the remaining two-dimensional space we then evaluate  $E_{\text{BO}}$  along the curve  $q_{1,\min}(q_2)$ . This curve maps  $q_2$  to the particular  $q_1$  for which  $E_{\text{BO}}(\Omega; q_1, q_2, q_3 = 0, q_4 = 0)$  is minimal. This we do for three different  $\Omega$  [yellow markers in Fig. 3(b)], which results in the solid, the dashed, and the dash-dotted line in Fig. 3(a).